Journal of Power Sources 206 (2012) 230–235

Contents lists available at SciVerse ScienceDirect

Journal of Power Sources

journal homepage: www.elsevier.com/locate/jpowsour

High performance of $LiNi_{0.5}Mn_{0.5}O_2$ positive electrode boosted by ordered three-dimensional nanostructures

Yumin Liu [a,b], Feng Cao [a], Bolei Chen [b], Xingzhong Zhao [b], Steven L. Suib [c], Helen L.W. Chan [a], Jikang Yuan [a,*]

[a] Department of Applied Physics, the Hong Kong Polytechnic University, Hong Kong, China
[b] School of Physics and Technology, Wuhan University, Wuhan, China
[c] Department of Chemistry, the University of Connecticut, 55 North Eagleville Road, Storrs, CT 06269-3060, USA

ARTICLE INFO

Article history:
Received 29 September 2011
Received in revised form
29 December 2011
Accepted 10 January 2012
Available online 18 January 2012

Keywords:
Three-dimensional nanostructure
In situ conversion
Lithium nickel manganese oxide
Positive electrode materials
Electrochemical performance
Lithium-ion battery

ABSTRACT

Three-dimensional $LiNi_{0.5}Mn_{0.5}O_2$ (3D-$LiNi_{0.5}Mn_{0.5}O_2$) nanostructures are *in situ* prepared using cryptomelane-type octahedral molecular sieve manganese dioxide (OMS-2) in the form of dendritic nanostructures as templates. The complete conversion of the OMS-2 precursor to layered α-$NaFeO_2$-type $LiNi_{0.5}Mn_{0.5}O_2$ and the retention of the 3D dendritic nanostructures have been confirmed by XRD, FE-SEM, TEM, and HR-TEM. The as-synthesized nanostructured positive electrode exhibits a significant improvement in rate performance and cycling reversibility due to its unique nanostructures composed of single-crystalline $LiNi_{0.5}Mn_{0.5}O_2$ nanorods. And the influence of the assembly mode of nanosize $LiNi_{0.5}Mn_{0.5}O_2$ positive electrode material to its electrochemical performances has been investigated. The battery based on 3D-$LiNi_{0.5}Mn_{0.5}O_2$ retains a discharge capacity of 151.6 mAh g^{-1} (93% of the first discharge capacity) after 50 cycles. A specific discharge capacity of 141.8 mAh g^{-1} was retained at a rate of 3.2 C, which is about 80% of the capacity at a rate of 0.2 C.

1. Introduction

Rechargeable lithium-ion batteries are one of the most successful power sources that are vital to meet the challenge of global warming and the limited and unrecyclable nature of fossil fuels. Rechargeable batteries have been considered as prime candidates to power the next generation of plug-in hybrid electric and electric vehicles (P-HEVs and EVs), which require high energy and power density [1,2]. To achieve this goal that is essential to meet future challenges of energy storage, the design and fabrication of new materials, especially in the form of new nanostructured materials, is critical. Due to their reduced dimensions, nanostructured positive and negative electrode can enable far higher intercalation/deintercalation rates, thus high power output will be generated [3–5]. However, nanomaterials, when used as positive and negative electrode in lithium batteries, have their inherent shortcomings. There are several disadvantages for employment of nanomaterials in lithium-ion batteries. For example, nanostructured positive and negative electrodes are generally difficult to prepare, and their dimensions and morphologies are hard to control. It is also difficult to ensure good electronic contact among nanoparticles due to expansion and contraction during intercalation/deintercalation [4,5]. Thus, it is essential to design and fabricate nanostructured positive and negative electrodes with well-defined morphologies for high electrochemical performance. Recently, nanostructured positive electrode materials in lithium-ion batteries have been investigated in order to achieve a considerable improvement in cycling performance and to increase the rate (power) of the batteries [6–9]. Nevertheless, due to difficulty encountered in accurate control over synthetic parameters such as temperature and ratios of precursors, the architecture of ternary and quaternary 3D nanostructured positive electrodes for lithium-ion batteries is less developed.

Due to its high Li^+ mobility, high electrochemical potential versus Li/Li^+ (~4 V), and a practical capacity of above 140 mAh g^{-1} with a good reversibility [10], $LiCoO_2$ has been investigated as positive electrode materials in rechargeable lithium-ion batteries for nearly two decades. However, restricted by high cost and toxicity of cobalt compounds, it is urgent and extremely important to find cheap, environmental-benign positive electrode materials to replace $LiCoO_2$ [11].

Among promising candidates of positive electrode materials in lithium battery, lithium manganate positive electrode materials with layered $LiMnO_2$ and spinel-type $LiMn_2O_4$ have been studied as candidates to replace $LiCoO_2$ [12,13]. Compared to $LiCoO_2$, lithium manganate positive electrode materials demonstrate lower cost

* Corresponding author. Tel.: +852 2766 5685; fax: +852 2333 7629.
E-mail address: apjkyuan@inet.polyu.edu.hk (J. Yuan).

0378-7753/$ – see front matter © 2012 Elsevier B.V. All rights reserved.
doi:10.1016/j.jpowsour.2012.01.069

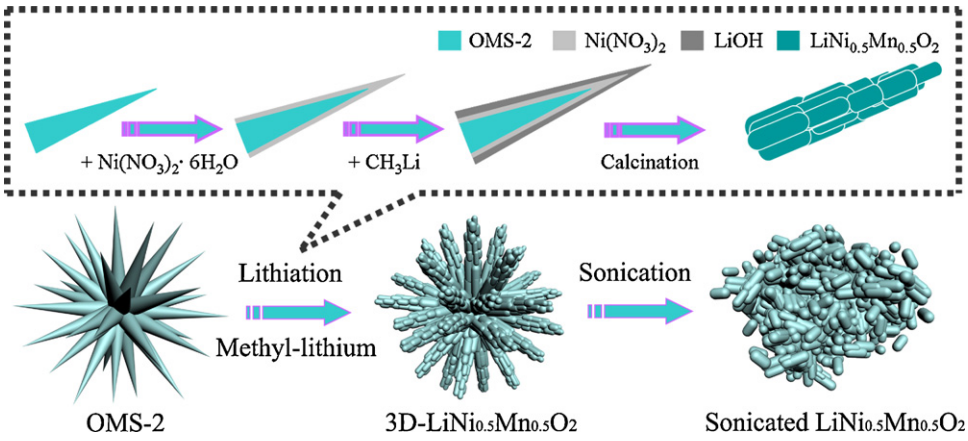

Scheme 1. Schematic representation of the *in situ* synthesis process.

and toxicity. However, $LiMn_2O_4$ have a spinel structure with three-dimensional channels. It is difficult for Li^+ to diffuse in $LiMn_2O_4$ positive electrode, thus, $LiMn_2O_4$ has a smaller capacity compared to that of $LiCoO_2$. On the other hand, layered $LiMnO_2$ is not thermodynamically stable [11]. Hence, $LiMnO_2$ has to be doped with nickel or cobalt in order to stabilize its layered structure during electrochemical process in lithium battery. The doped $LiNi_xMn_{1-x}O_2$ positive electrode materials have nearly all the advantages of $LiCoO_2$ without use of cobalt. Furthermore, $LiNi_xMn_{1-x}O_2$ exhibits higher theoretical capacity and apparently better thermodynamical stability compared to $LiMn_2O_4$ and $LiMnO_2$ electrodes [14]. However, both $LiCoO_2$ and $LiNi_xMn_{1-x}O_2$ materials commonly demonstrate a large degree of cation disorder originated from their α-$NaFeO_2$-type layered structure. Introduction of metal atoms into the Li^+ layers will disrupt the Li^+ pathways and hold neighboring transition-metal slab together, thus leading to reduced Li^+ mobility and rate performance [15]. $LiNi_xMn_{1-x}O_2$ materials were first reported by Ohzuku and Makimura in 2001 [16]. Many efforts have been made to synthesize $LiNi_xMn_{1-x}O_2$ materials with well-ordered structures [17–19]. It has been reported that the mixed-hydroxide or co-precipitation method may be best to prepare $LiNi_xMn_{1-x}O_2$ materials [20,21]. However, it is difficult to synthesize $LiNi_xMn_{1-x}O_2$ with the unique nanostructures by this method. Preparation of positive electrode materials with a high rate and large electrode capacity by direct nanoarchitectured technology still remains a challenge.

In our previous work, we have synthesized nanostructured $LiNi_{0.5}Mn_{0.5}O_2$ spheres via a facile lithiation method using γ-MnO_2 as template [22]. The battery based on this nanostructured positive electrode material exhibits an improvement of high rate performance compared with that based on micrometre $LiNi_{0.5}Mn_{0.5}O_2$ particles prepared by a conventional solid-state reaction method. Herein, we have successfully synthesized $LiNi_{0.5}Mn_{0.5}O_2$ with more ordered three-dimensional nanostructures via an *in situ* conversion of cyptomelane-type manganese oxide (OMS-2) dendritic nanostructures. Furthermore, we provided the direct evidence that the assembly mode of nanosize $LiNi_{0.5}Mn_{0.5}O_2$ positive electrode material is crucial to its electrochemical performances.

The as-synthesized OMS-2 dendritic nanostructures were prepared via a hydrothermal reaction. The microstructures and morphologies of OMS-2 nanodendrite and 3D nanostructured $LiNi_{0.5}Mn_{0.5}O_2$ (3D-$LiNi_{0.5}Mn_{0.5}O_2$) are characterized by X-ray diffraction (XRD), field emission scanning electron microscopy (FESEM), transmission electron microscopy (TEM), and energy dispersive X-ray spectroscopy (EDX). Electrochemical performances of the batteries based on 3D-$LiNi_{0.5}Mn_{0.5}O_2$ are also reported.

2. Experimental details

2.1. Synthesis of OMS-2 three-dimensional manganese dioxides

Manganese dioxides with ordered 3D nanostructures were synthesized by a hydrothermal method. The following equation shows the chemical reaction in out system:

$$2NaClO_3\,(aq) + 6MnSO_4\,(aq) + 6H_2O = 6MnO_2\,(s) + Na_2SO_4\,(aq) + 2HCl\,(l) + 5H_2SO_4\,(l)$$

8 mmol $NaClO_3$ and 8 mmol $MnSO_4{\cdot}H_2O$ were mixed with 65 mL deionized (DI) water, followed by an addition of 1 mL condensed H_2SO_4. A clear and uniform solution was obtained after vigorous stirring at room temperature for half an hour. The clear solution was then transferred to a 125 mL Teflon-lined autoclave. The autoclave was sealed and heated at 180 °C for 12 h. The resulting black slurry was rinsed with DI water several times in order to remove soluble impurities. The product was dried in an oven at 120 °C overnight.

2.2. Synthesis of ordered 3D-$LiNi_{0.5}Mn_{0.5}O_2$

3D-$LiNi_{0.5}Mn_{0.5}O_2$ was obtained by the following steps: 5 mmol $Ni(NO_3)_2{\cdot}6H_2O$ were first dissolved in 100 mL distilled water, and then 5 mmol as-synthesized 3D OMS-2 was added to this solution by vigorously stirring at room temperature to form a homogeneous mixture followed by evaporation of the solvent at 120 °C on a hotplate. The well-mixed powder was transferred into 50 mL diethyl

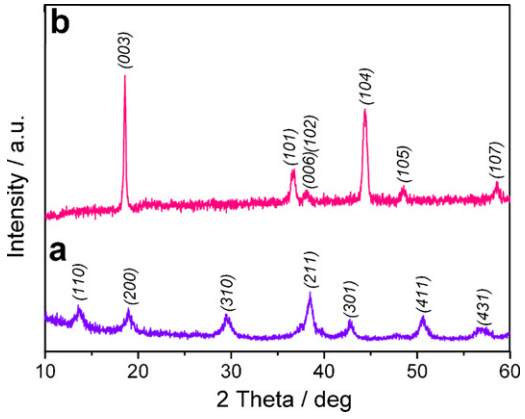

Fig. 1. X-ray diffraction patterns (Cu Kα radiation) of (a) as-prepared OMS-2; and (b) 3D-$LiNi_{0.5}Mn_{0.5}O_2$.

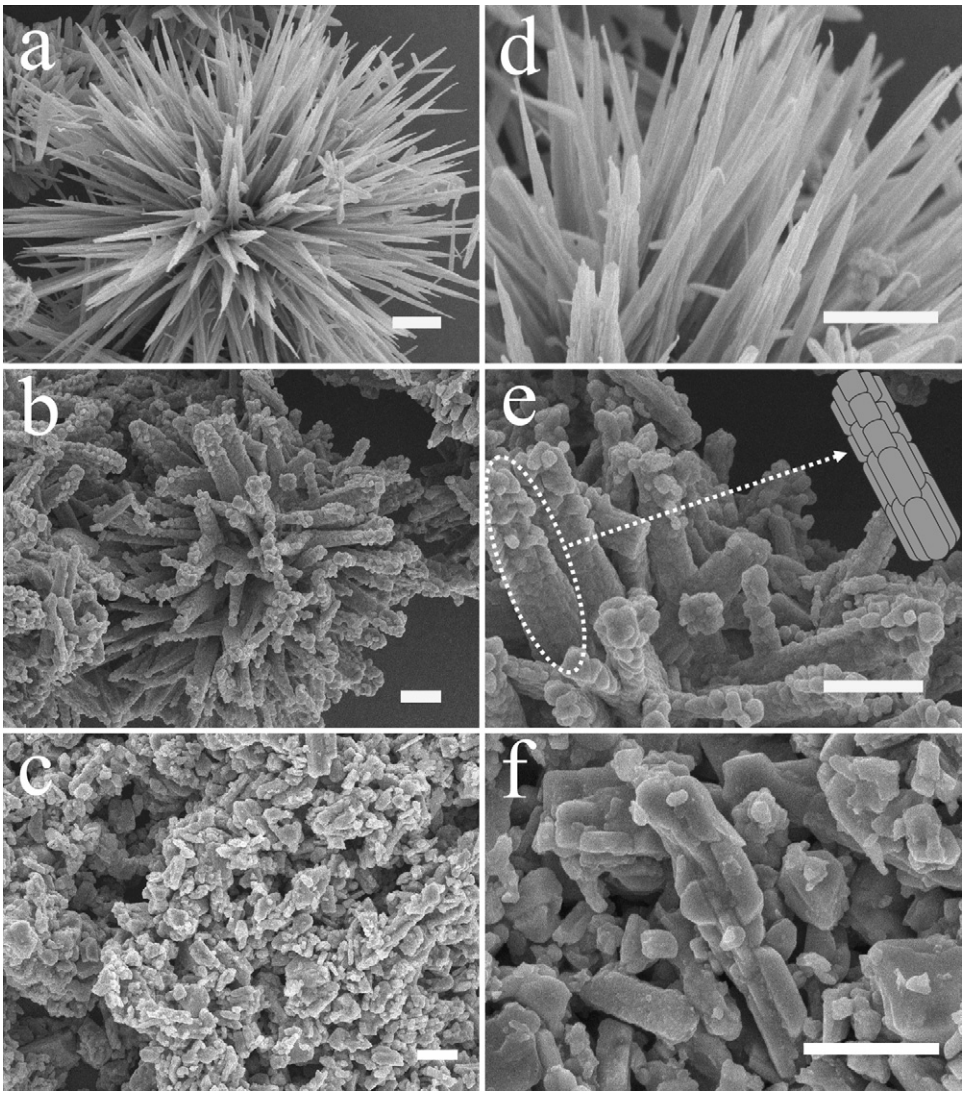

Fig. 2. SEM images of (a and d) nanodendritic OMS-2, (b and e) 3D-$LiNi_{0.5}Mn_{0.5}O_2$ (800 °C), and (c and f) Sonicated $LiNi_{0.5}Mn_{0.5}O_2$. All scale bars are 1 μm. Inset in (e) shows a schematic morphology of aggregate of $LiNi_{0.5}Mn_{0.5}O_2$ nanorods.

ether solution by vigorously stirring, and then 10 mmol CH_3Li were added to this solution dropwise followed by evaporation of the solvent at room temperature. The resulted powder was transferred to a furnace and calcined at 800 °C for 5 h. $LiNi_{0.5}Mn_{0.5}O_2$ was also synthesized as a control group through a conventional solid-state reaction based on literature [21].

2.3. Characterization

The crystalline phase of the prepared nanomaterials was indentified by X-ray diffraction (XRD) using a Philips Xpert XRD System with Cu Kα radiation (λ = 1.54056 Å). The diffraction data were obtained at 2θ = 10–60°, with a step size of 0.02°. The morphology of 3D OMS-2 and $LiNi_{0.5}Mn_{0.5}O_2$ was observed by field emission scanning electron microscopy (FESEM, JSM 6335F). TEM and HRTEM investigations were carried out using a JEOL 2010, equipped with an energy dispersive X-ray analysis (EDX) system.

2.4. Electrochemical characterization

Electrochemical performances were conducted using 2032 coin-type half-cells that were assembled in a glove box filled with argon gas. We made the positive electrodes for the battery test cells from the active material (3D-$LiNi_{0.5}Mn_{0.5}O_2$, sonicated $LiNi_{0.5}Mn_{0.5}O_2$, and SS-$LiNi_{0.5}Mn_{0.5}O_2$), carbon black, and a poly(vinyl difluoride) binder in a weight ratio of 70:20:10. And then the slurry was prepared by thoroughly mixing a N-methyl-2-pyrrolidene solution with the as-prepared active material, carbon black, and poly(vinyl difluoride) binder. The resulting slurry was coated on an aluminum foil and roll-pressed. The entire assembly was dried under vacuum at 120 °C overnight. Pure lithium foil was used as negative electrode and a polypropylene separator (Celgard) was used to separate the positive and negative electrode. The electrolyte consisted of a solution of 1.0 M $LiPF_6$ in ethylene carbonate (EC)/dimethyl carbonate (DMC) (1:1, in volume) obtained from Shenzhen Kejing Instrument Co. Ltd. The discharge and charge measurement were carried out on a Land test system in a voltage window of 2.5–4.2 V at room temperature with different rates.

3. Results and discussion

XRD patterns of as-prepared OMS-2 and $LiNi_{0.5}Mn_{0.5}O_2$ nanoparticles are shown in Fig. 1. All observed peaks shown in Fig. 1a can be indexed to a pure tetragonal cryptomelane-type (OMS-2) phase. XRD pattern shown in Fig. 1b indicates a pure α-$NaFeO_2$-type $LiNi_{0.5}Mn_{0.5}O_2$. In comparison with conventional

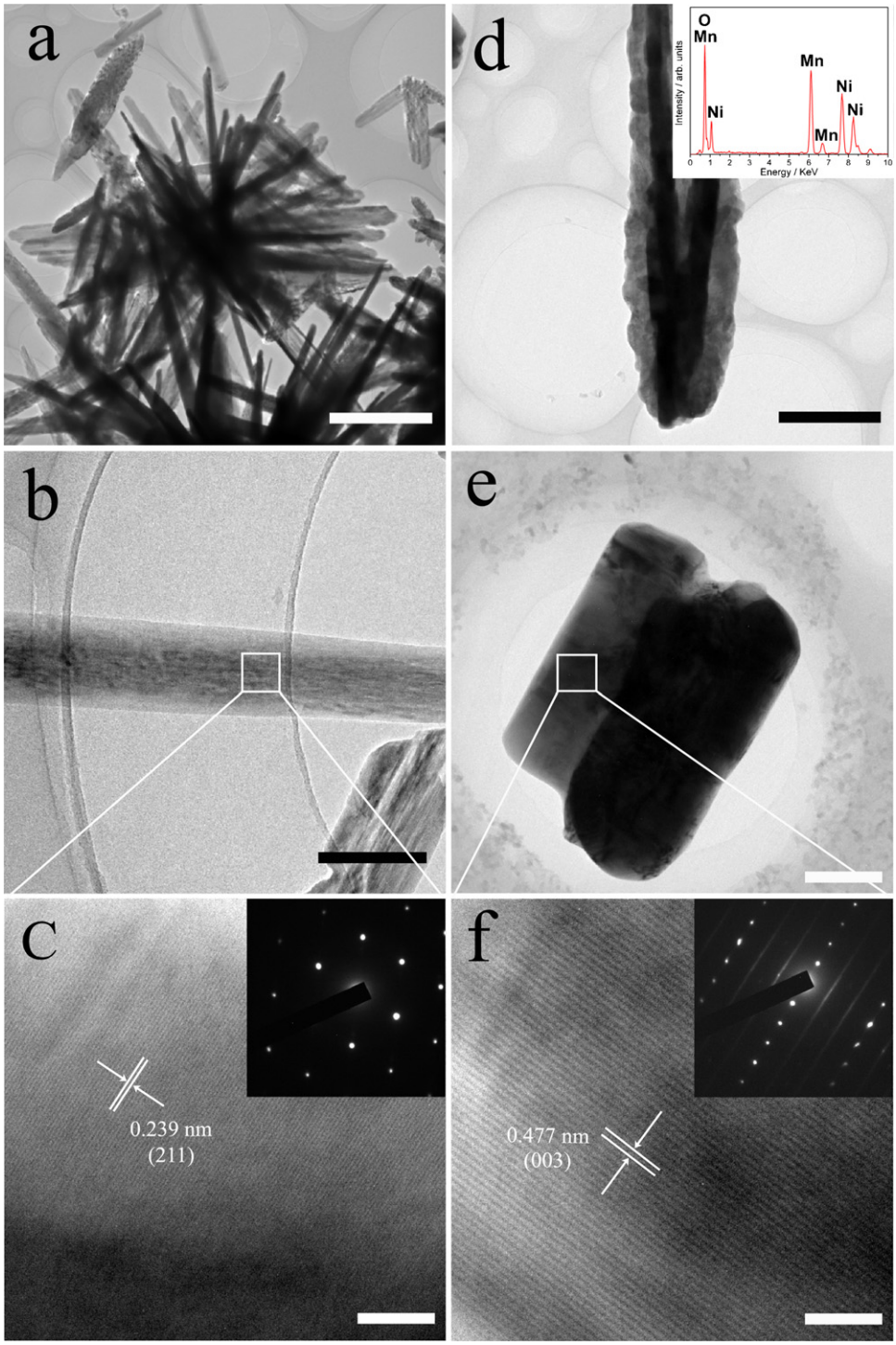

Fig. 3. Selected area TEM and HR-TEM images of: (a)–(c) OMS-2 nanodentrite; (d)–(f) 3D-$LiNi_{0.5}Mn_{0.5}O_2$ (800 °C). Insets of (c) and (f) electron diffraction patterns of OMS-2 and 3D-$LiNi_{0.5}Mn_{0.5}O_2$, respectively. Scale bars are 1 μm, 1 μm, 100 nm, 200 nm, 5 nm, and 5 nm, respectively. Inset of (d) shows EDX pattern of 3D-$LiNi_{0.5}Mn_{0.5}O_2$ nanorod.

method of synthesizing $LiNi_{0.5}Mn_{0.5}O_2$, the lower calcination temperature (800 °C) for preparation of our samples and resulted ordered 3D structures can be attributed to the formation of homogeneous lithium hydroxide thin film originated from decomposition of methyl-lithium on the surface of dendritic OMS-2 precursors (Scheme 1). Unit cell parameters of $a = b = 2.86$ Å and $c = 14.28$ Å for $LiNi_{0.5}Mn_{0.5}O_2$ were calculated from the XRD patterns, which are in good agreement with literatures [15,21,23]. Compared with previous literatures, we can see that there are also some "cation-mixing" exists, due to displacement between the transition metal ions and lithium ions [19]. The morphologies of as-synthesized 3D OMS-2 were obtained by field emission scanning electron microscopy (FESEM). Fig. 2a shows a dendritic morphology composes of individual OMS-2 nanorods with sharp tips. The diameter of each OMS-2 nanorod is about 100 nm (Fig. 2d). The 3D nanostructures of $LiNi_{0.5}Mn_{0.5}O_2$ are revealed in Fig. 2b. Similarities between morphologies of precursor (OMS-2) and final product ($LiNi_{0.5}Mn_{0.5}O_2$) confirm an *in situ* conversion during calcination.

SEM image with high magnification also shows that each branch of the nanodendritic $LiNi_{0.5}Mn_{0.5}O_2$ composes of ordered aggregate of small $LiNi_{0.5}Mn_{0.5}O_2$ nanorods (Fig. 2e).

The as-prepared 3D OMS-2 and final 3D-$LiNi_{0.5}Mn_{0.5}O_2$ were further characterized by transmission electron microscopy (TEM), as shown in Fig. 3. Fig. 3a shows a typical TEM image for OMS-2 nanodendrite, and a selected nanorod located in a branch of OMS-2 is shown in Fig. 3b. The lattice fringes were clearly observed from a high-resolution TEM (HR-TEM) image, as shown in Fig. 3c. The distance between neighboring lattice fringes is about 2.39 Å, corresponding to the (2 1 1) planes of cyptomelane-type OMS-2. Further investigation of electron diffraction demonstrates that the 3D OMS-2 composes of single-crystalline nanorods (Fig. 3c, inset). Fig. 3d shows the TEM image of 3D-$LiNi_{0.5}Mn_{0.5}O_2$ nanodendrite, and a selected nanorod from 3D-$LiNi_{0.5}Mn_{0.5}O_2$ is shown in Fig. 3e. The width of 4.77 Å between neighboring fringes of $LiNi_{0.5}Mn_{0.5}O_2$ nanorods corresponds to the (0 0 3) planes (Fig. 3f). Electron diffraction pattern of individual $LiNi_{0.5}Mn_{0.5}O_2$ nanorod and the clear lattice fringes show that the 3D-$LiNi_{0.5}Mn_{0.5}O_2$ also composes of single-crystalline nanorods (Fig. 3f, inset). Energy-dispersive X-ray analysis (EDX) results confirm presence of both Mn and Ni elements contained in $LiNi_{0.5}Mn_{0.5}O_2$ nanorods (Fig. 3d, inset).

The electrochemical performances of the batteries based on 3D-$LiNi_{0.5}Mn_{0.5}O_2$ positive electrodes were investigated by cycling at room temperature from a coin-type half cell using Li metal as negative electrode. Representative charge–discharge profiles of 3D-$LiNi_{0.5}Mn_{0.5}O_2$ positive electrode with 50 cycles at a rate of 0.2 C (36 mA g^{-1}) in the potential range of 2.5/4.2 V were shown in Fig. 4a. A flattening plateau around 3.7 V was observed, representing a typical electrochemical behavior of layered $LiNi_{0.5}Mn_{0.5}O_2$ [15,20,24]. The 3D-$LiNi_{0.5}Mn_{0.5}O_2$ exhibited a discharge capacity of 162, 167, 174, 176, 165, and 150 mAh g^{-1} (±1 mAh g^{-1}) when the cycle number was 1, 2, 5, 10, 30, and 50, respectively. The discharge capacity had dramatically increased from 162 mAh g^{-1} to 176 mAh g^{-1} (±1 mAh g^{-1}) after 10 cycles. The increase of capacity can be attributed to the tendency of stabilization of 3D-$LiNi_{0.5}Mn_{0.5}O_2$ nanoparticles after several cycles. After 50 cycles, a discharge capacity of 150 mAh g^{-1} (±1 mAh g^{-1}) was retained, which was about 93% of the first discharge capacity. Cyclic voltammogram (CV) of 3D-$LiNi_{0.5}Mn_{0.5}O_2$ electrode for the initial cycle was performed by scanning from a potential of 2.5 V to an upper limit of 4.5 V versus Li/Li^+ at a scan rate of 0.1 mV s^{-1} (Fig. 4b). The shapes of the CV curves were similar to those reported by other research groups [25]. It can be seen from the CV curves that two major current peaks appeared around potentials (V versus Li/Li^+) of 3.72 and 3.94 V, both of which could be attributed to the redox reactions of Ni^{2+}/Ni^{3+} and/or Ni^{2+}/Ni^{4+} [23,26]. And there are two minor anodic and cathodic peaks at 4.45 and 4.25 V, respectively. It can be seen that the areas under the peaks in the region of 4.25–4.45 are much smaller than those between 3.72 and 3.94. Thus the minor peaks are not due to the $Ni^{3+/4+}$ couple, they are possible resulted from a reversible structural transition [27]. To further investigate the performance of 3D-$LiNi_{0.5}Mn_{0.5}O_2$ in higher current rates, the battery was cycled at different rates ranging from 0.2 C (36 mA g^{-1}) to 3.2 C (576 mA g^{-1}) (Fig. 5a). The 3D-$LiNi_{0.5}Mn_{0.5}O_2$ positive electrode delivers discharge capacity of about 177, 170, 163, 154, and 142 mAh g^{-1} (±1 mAh g^{-1}) at a rate of 0.2 C, 0.6 C, 1.6 C, 2.4 C, and 3.2 C, respectively. Remarkably, the pseudoplateau was still above 3.6 V at a rate of 3.2 C, and a specific discharge capacity of 142 mAh g^{-1} (±1 mAh g^{-1}) (about 80% of the capacity at a rate of 0.2 C) was retained. To investigate the advantages of this ordered 3D nanostructure, we destructed the 3D-$LiNi_{0.5}Mn_{0.5}O_2$ nanostructures by sonication, through which random aggregates of $LiNi_{0.5}Mn_{0.5}O_2$ nanorods were formed (Fig. 2c and f). The electrochemical performance of $LiNi_{0.5}Mn_{0.5}O_2$ positive electrode after sonication was tested under the same conditions. Cycling performance of batteries based on 3D-$LiNi_{0.5}Mn_{0.5}O_2$ and its sonicated counterpart were tested at a rate of 0.2 C in the voltage range of 2.5–4.2 V (Fig. 4c). It can be seen that 3D-$LiNi_{0.5}Mn_{0.5}O_2$ positive electrode has a better stability over repeated cycling than that of the sonicated $LiNi_{0.5}Mn_{0.5}O_2$ positive electrode. We also compared the high rate performance of 3D-$LiNi_{0.5}Mn_{0.5}O_2$ positive electrode with that of sonicated $LiNi_{0.5}Mn_{0.5}O_2$ and $LiNi_{0.5}Mn_{0.5}O_2$ synthesized by a conventional solid-state reaction method (SS-$LiNi_{0.5}Mn_{0.5}O_2$). All of the batteries were examined under the same conditions. Galvanostatic cycling of batteries based on 3D-$LiNi_{0.5}Mn_{0.5}O_2$, sonicated $LiNi_{0.5}Mn_{0.5}O_2$, and SS-$LiNi_{0.5}Mn_{0.5}O_2$ at rates ranging from 0.2 C to 3.2 C were shown in Fig. 5b. It can be seen that a remarkable degradation of discharge capacity was observed when using

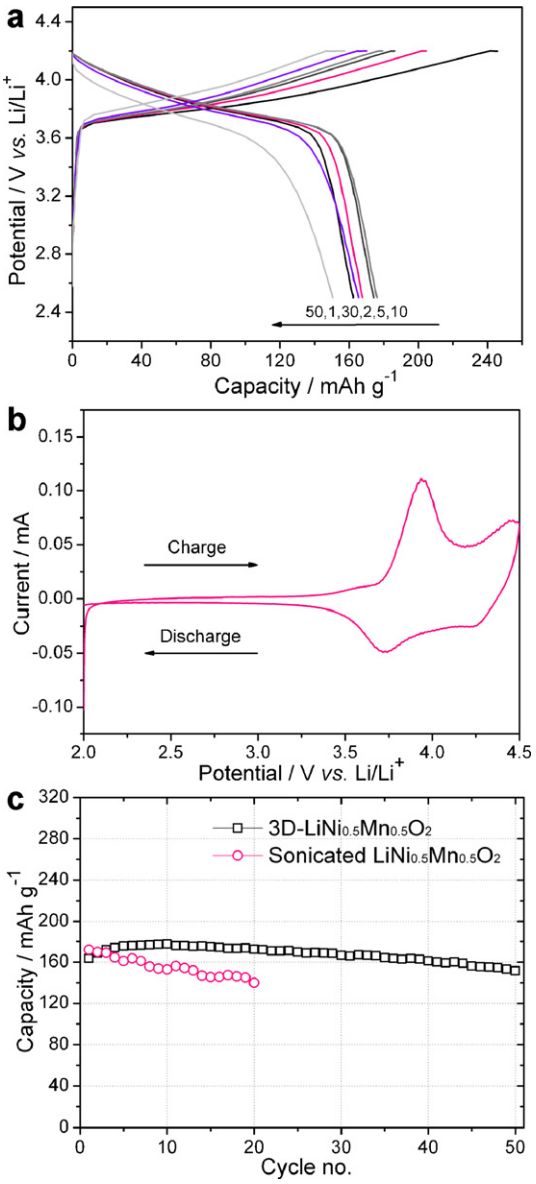

Fig. 4. (a) Charge–discharge galvanostatic curves for 3D-$LiNi_{0.5}Mn_{0.5}O_2$ cycled at room temperature obtained from a 2032 coin-type half cell using Li metal as negative at a rate of 0.2 C in the voltage range of 2.5–4.2 V. (b) Cyclic voltammogram of 3D-$LiNi_{0.5}Mn_{0.5}O_2$ positive electrode for the initial cycle at a scan rate of 0.1 mV s^{-1}. (c) Cycling performance of the batteries based on 3D-$LiNi_{0.5}Mn_{0.5}O_2$ and sonicated $LiNi_{0.5}Mn_{0.5}O_2$ at a rate of 0.2 C.

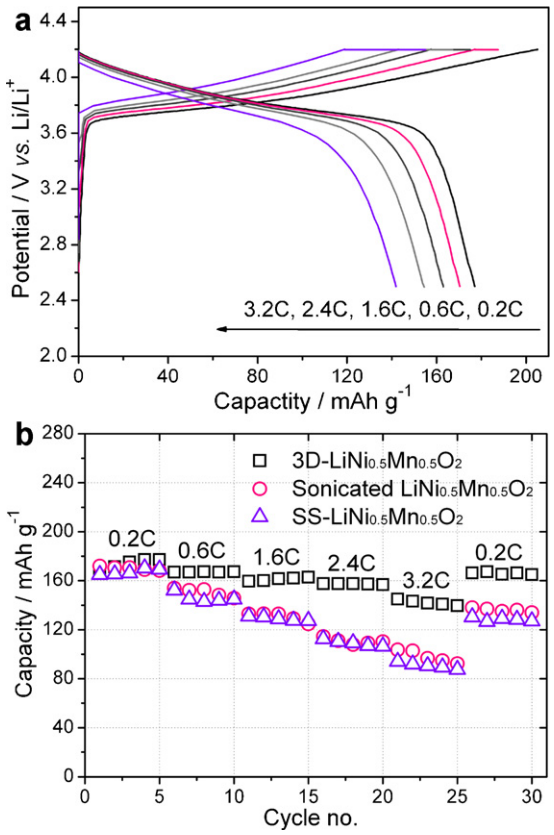

Fig. 5. (a) Rate capability of 3D-$LiNi_{0.5}Mn_{0.5}O_2$ with increasing rates from 0.2 C to 3.2 C between 2.5 and 4.2 V. (b) Galvanostatic cycling of batteries based on 3D-$LiNi_{0.5}Mn_{0.5}O_2$, sonicated $LiNi_{0.5}Mn_{0.5}O_2$, and SS-$LiNi_{0.5}Mn_{0.5}O_2$ at rates ranging from 0.2 C to 3.2 C in the same voltage window of 2.5–4.2 V.

sonicated $LiNi_{0.5}Mn_{0.5}O_2$ and SS-$LiNi_{0.5}Mn_{0.5}O_2$ as positive electrodes, whereas 3D-$LiNi_{0.5}Mn_{0.5}O_2$ positive electrode shows an obviously lower fading rate than the first two materials, indicating a higher stability during cycling at high rates. These results for $LiNi_{0.5}Mn_{0.5}O_2$ synthesized by a conventional solid-state reaction were in good agreement with previous reports [24]. Based on these comparisons, we can conclude that 3D-$LiNi_{0.5}Mn_{0.5}O_2$ positive electrode substantially improved its electrochemical performance. The improved performance of 3D-$LiNi_{0.5}Mn_{0.5}O_2$ electrode can be attributed to the reduced dimensions of positive electrode nanoparticles that enable far higher lithium insertion/removal rates and faster interfacial kinetics, and to the ordered 3D nanodendritic structures of $LiNi_{0.5}Mn_{0.5}O_2$ which improves the contacts among individual $LiNi_{0.5}Mn_{0.5}O_2$ nanorods during expansion and contraction caused by insertion/removal of lithium ion. The improvement of electrochemical performance can also be attributed to the single crystallinity of $LiNi_{0.5}Mn_{0.5}O_2$ nanorods. Since single crystalline positive electrode materials show higher structural stability and contain less defects [28,29], higher capacity and rate capability can be obtained using single crystalline positive electrode materials compared with polycrystalline positive electrode materials.

4. Conclusion

In conclusion, we have successfully synthesized ordered 3D nanodendritic $LiNi_{0.5}Mn_{0.5}O_2$ using as-prepared OMS-2 dendritic nanostructure as template. The complete conversion of OMS-2 precursor to layered α-$NaFeO_2$-type $LiNi_{0.5}Mn_{0.5}O_2$ and the retention of the 3D dendritic nanostructures have been confirmed by XRD, FE-SEM, TEM, and HR-TEM. This 3D-$LiNi_{0.5}Mn_{0.5}O_2$ positive electrode exhibits a remarkable enhancement of cycling reversibility and rate performance. The improvement of electrochemical performance can be attributed to the formation of ordered 3D dendritic nanostructures of $LiNi_{0.5}Mn_{0.5}O_2$ composed of single crystalline $LiNi_{0.5}Mn_{0.5}O_2$ nanorods. The methodology of synthesizing $LiNi_{0.5}Mn_{0.5}O_2$ with ordered 3D nanostructures can be extended to preparation of spinel positive electrode structures by employing manganese dioxide OMS nanoparticles with various morphologies as templates via similar *in situ* conversion route. Furthermore, it is possible to prepare nanostructured lithium nickel manganese oxide materials with high degree of cation order by optimizing synthetic conditions. Based on this nanoarchitechured technology, lithium nickel manganese oxide materials may be promising candidates for positive electrode materials in lithium-ion batteries.

Acknowledgement

This project was funded by The Hong Kong Polytechnic University Research Fund (Grant No. G-YH82).

References

[1] M. Armand, J.M. Tarascon, Nature 451 (2008) 652.
[2] M.S. Whittingham, Chem. Rev. 104 (2004) 4271.
[3] D.W. Liu, G.Z. Cao, Energy Environ. Sci. 3 (2010) 1218–1237.
[4] P.G. Bruce, B. Scrosati, J.-M. Tarascon, Angew. Chem. Int. Ed. 47 (2008) 2930.
[5] A.S. Aricò, P.G. Bruce, B. Scrosati, J.-M. Tarascon, W. Van Schalkwijc, Nat. Mater. 4 (2005) 366.
[6] F. Jiao, K.M. Shaju, P.G. Bruce, Angew. Chem. Int. Ed. 44 (2005) 6550.
[7] J.-Y. Luo, H.-M. Xiong, Y.-Y. Xia, J. Phys. Chem. C 112 (2008) 12051.
[8] E. Hosono, T. Kudo, I. Honma, H. Matsuda, H.S. Zhou, Nano Lett. 9 (2009) 1045.
[9] D.K. Kim, P. Muralidharan, H.-W. Lee, R. Ruffo, Y. Yang, C.K. Chan, H.L. Peng, R.A. Huggins, Y. Cui, Nano Lett. 8 (2008) 3948.
[10] M. Winter, J.O. Besenhard, M.E. Spahr, P. Novák, Adv. Mater. 10 (1998) 725.
[11] B. Ammundsen, J. Paulsen, Adv. Mater. 13 (2001) 943.
[12] A.R. Armstrong, P.G. Bruce, Nature 499 (1996) 381.
[13] M.M. Hackeray, W.I.F. David, P.G. Bruce, J.B. Goodenough, Mater. Res. Bull. 18 (1983) 461.
[14] B.L. Ellis, K.T. Lee, L.F. Nazar, Chem. Mater. 22 (2010) 691.
[15] S.B. Schougaard, J. Bréger, M. Jiang, C.P. Grey, J.B. Goodenough, Adv. Mater. 18 (2006) 905.
[16] T. Ohzuku, Y. Makimura, Chem. Lett. 8 (2001) 744.
[17] Z.H. Lu, L.Y. Beaulieu, R.A. Donaberger, C.L. Thomas, J.R. Dahn, J. Electrochem. Soc. 149 (2002) A778.
[18] K.M. Shaju, G.V. Subba Rao, B.V.R. Chowdari, Electrochim. Acta 48 (2003) 1505.
[19] M.V. Reddy, G.V. Subba Rao, B.V.R. Chowdari, Electrochim. Acta 50 (2005) 3375.
[20] Y. Makimura, T. Ohzuku, J. Power Sources 119–121 (2003) 156.
[21] Z.-H. Lu, D.D. MacNeil, J.R. Dahn, Electrochem. Solid-State Lett. 4 (2001) A191.
[22] Y.M. Liu, B.L. Chen, F. Cao, X.Z. Zhao, J.K. Yuan, J. Mater. Chem. 21 (2011) 10437.
[23] B.-J. Hwang, T.-H. Yu, M.-Y. Cheng, R. Santhanam, J. Mater. Chem. 19 (2009) 4536.
[24] K. Kang, Y.S. Meng, J. Bréger, C.P. Grey, G. Ceder, Science 311 (2006) 977.
[25] M. Yoncheva, R. Stoyanova, E. Zhecheva, R. Alcántara, G. Ortiz, J.L. Tirado, Electrochim. Acta 54 (2009) 1694.
[26] S.-H. Kang, J. Kim, M.E. Stoll, D. Abraham, Y.K. Sun, K. Amine, J. Power Sources 112 (2002) 41.
[27] M.V. Reddy, G.V. Subba Rao, B.V.R. Chowdari, J. Power Sources 160 (2006) 1369.
[28] Y. Wang, G.Z. Cao, Adv. Mater. 20 (2008) 2251.
[29] X.Y. Han, Q.F. Meng, T.L. Sun, J.T. Sun, J. Power Sources 195 (2010) 3047.